



**HAL**  
open science

## Line-field confocal time-domain optical coherence tomography with dynamic focusing

Arnaud Dubois, Olivier Levecq, Hicham Azimani, Arthur Davis, Jonas Ogien,  
David Siret, Anaïs Barut

► **To cite this version:**

Arnaud Dubois, Olivier Levecq, Hicham Azimani, Arthur Davis, Jonas Ogien, et al.. Line-field confocal time-domain optical coherence tomography with dynamic focusing. *Optics Express*, 2018, 26 (26), pp.33534. 10.1364/oe.26.033534 . hal-01950735

**HAL Id: hal-01950735**

**<https://hal-iogs.archives-ouvertes.fr/hal-01950735>**

Submitted on 11 Dec 2018

**HAL** is a multi-disciplinary open access archive for the deposit and dissemination of scientific research documents, whether they are published or not. The documents may come from teaching and research institutions in France or abroad, or from public or private research centers.

L'archive ouverte pluridisciplinaire **HAL**, est destinée au dépôt et à la diffusion de documents scientifiques de niveau recherche, publiés ou non, émanant des établissements d'enseignement et de recherche français ou étrangers, des laboratoires publics ou privés.



# Line-field confocal time-domain optical coherence tomography with dynamic focusing

ARNAUD DUBOIS,<sup>1,\*</sup> OLIVIER LEVECQ,<sup>2</sup> HICHAM AZIMANI,<sup>2</sup>  
ARTHUR DAVIS,<sup>1,2</sup> JONAS OGIEN,<sup>1,2</sup> DAVID SIRET,<sup>2</sup> AND ANAÏS BARUT<sup>2</sup>

<sup>1</sup>Laboratoire Charles Fabry, Institut d'Optique Graduate School, Univ. Paris-Saclay, 91127 Palaiseau Cedex, France

<sup>2</sup>DAMAE Medical, 28 rue de Turbigo, 75003 Paris, France

\*arnaud.dubois@institutoptique.fr

**Abstract:** A time-domain optical coherence tomography technique is introduced for high-resolution B-scan imaging in real-time. The technique is based on a two-beam interference microscope with line illumination and line detection using a broadband spatially coherent light source and a line-scan camera. Multiple (2048) A-scans are acquired in parallel by scanning the sample depth while adjusting the focus. Quasi-isotropic spatial resolution of  $1.3 \mu\text{m} \times 1.1 \mu\text{m}$  (lateral  $\times$  axial) is achieved. *In vivo* cellular-level resolution imaging of human skin is demonstrated at 10 frames per second with a penetration depth of  $\sim 500 \mu\text{m}$ .

©2018 Optical Society of America under the terms of the [OSA Open Access Publishing Agreement](#)

## 1. Introduction

Optical coherence tomography (OCT) is an established technique for cross-sectional imaging of biological tissues with micrometer-scale spatial resolution [1,2]. OCT is commonly employed in diverse medical applications [3], notably in ophthalmology to obtain high-resolution images of the retina and the anterior segment of the eye [4]. OCT has begun to be used in interventional cardiology [5], and in gastroenterology for the detection and diagnosis of cancers [6]. OCT also shows promise in dermatology to improve the diagnosis process of skin lesions [7].

Imaging at high spatial resolution with OCT is of particular interest to resolve subtle morphological changes of tissues for early diagnosis of diseases. Since the introduction of OCT, significant progress in the spatial resolution of OCT images has been achieved. The axial resolution in OCT is essentially governed by the temporal coherence of the illumination light source [2]. Gradual improvement of the axial resolution in OCT has been obtained by the emergence of efficient broadband light sources. Axial resolutions down to  $\sim 1 \mu\text{m}$  have been achieved in particular with mode-locked lasers [8] and more recently with supercontinuum lasers [9–11]. In conventional OCT, a B-scan image is obtained by lateral scanning of a light beam to acquire several adjacent A-scans. The imaging lateral resolution depends on how the light beam is focused on the sample. Depending on whether each A-scan is acquired as a function of the optical frequency (in frequency/Fourier-domain OCT, referred to as FD-OCT) or as a function of time (in time-domain OCT, referred to as TD-OCT), the beam focusing constraints differ, which impacts the lateral resolution that can be achieved.

In FD-OCT, all the backscattering structures of the sample located within the depth range of an A-scan contribute in parallel to the signal. A sufficiently large depth of field (DOF) is required, since the focus cannot be adjusted during the acquisition of each A-scan. Efforts have been made to minimize the resulting inherent limitation of lateral resolution in FD-OCT. The DOF can be increased by illuminating the sample with a Bessel beam [12,13], or by using phase masks [14]. Alternative methods based on computational imaging solutions have been proposed, including interferometric synthetic aperture microscopy [15] and digital refocusing [16–18]. Another approach consists of combining several B-scan images acquired at different depths in order to image over a depth range larger than the DOF. This approach

has been implemented using the Gabor-based fusion method [19] and by using multiple light beams focused at different depths [20]. Despite these advances, however, the imaging lateral resolution in FD-OCT is still limited to a few micrometers [17–19].

In conventional TD-OCT, the signal in each A-scan is acquired sequentially by scanning the length of the interferometer reference arm. Most TD-OCT devices have a large DOF to avoid the adjustment of the focus. However, in contrast to FD-OCT, it is conceptually possible in TD-OCT to continuously adjust the focus as a function of depth. Dynamically-focused TD-OCT devices have been reported, with improved lateral imaging resolution compared to conventional TD-OCT, but with the drawback of significantly reduced image acquisition speed or moderate detection sensitivity [21–24]. TD-OCT devices with partial adjustment of the focus have also been proposed. In [8] a sequence of images was acquired by gradually shifting the focus and the in-focus imaging zones were then fused together. In [25] multiple foci were collected simultaneously with a multifocus fiber tip array. In both cases, a trade-off was made between lateral resolution and image acquisition speed.

Alternatively, TD-OCT with lateral (transverse) priority scanning enables a slower translation of the focus at the image frame rate [26]. This approach, requiring faster lateral scanning, was demonstrated for *in vitro* biological tissue imaging, at 1 frame per second (fps) with a lateral resolution of 10  $\mu\text{m}$  [27].

Finally, although higher lateral resolution can be achieved by dynamic focusing in TD-OCT, real-time ultrahigh-resolution ( $\sim 1 \mu\text{m}$ ) B-scan imaging in highly scattering biological tissues has not been successfully demonstrated so far.

In this paper, we introduce a TD-OCT technique called line-field confocal optical coherence tomography (LC-OCT) that allows for producing B-scan images without the lateral resolution limitation of FD-OCT and without the speed limitation of conventional dynamically-focused TD-OCT. In LC-OCT, multiple A-scans are acquired in parallel using line illumination and line detection. A B-scan image can thus be obtained without lateral scanning of a light beam as required in conventional OCT. Since only one scan (depth scan) is required to acquire a B-scan image, this scan can be slower without increasing the acquisition time of the image. Continuous dynamic focusing is therefore facilitated. A high numerical aperture (NA) lens, such as a microscope objective, can be dynamically focused to produce images with high lateral resolution. By using a supercontinuum laser as a light source and balancing the optical dispersion in the interferometer arms, the axial resolution in LC-OCT reaches the best axial resolution achieved in OCT at a comparable central optical wavelength. Moreover, line illumination and detection combined with the use of a high NA objective provide an efficient confocal gate, which prevents most of unwanted scattered light from being detected. B-scan imaging at high resolution and in real-time in highly scattering tissues such as skin is demonstrated using LC-OCT.

## 2. Experimental setup

The schematic of our LC-OCT prototype is depicted in Fig. 1. It is based on a Linnik-type interferometer with two identical 0.5-NA water-immersion microscope objectives (MO1, MO2) (Olympus, UMPLFLN 20xW). The objective lens in the reference arm (MO1) is focused on the external surface of a glass plate (GP1), thus constituting a reference surface of  $\sim 4\%$  reflectivity. An identical glass plate (GP2) is placed in the sample arm in contact with the sample to image. The glass plates are made of fused silica and have a thickness of 500  $\mu\text{m}$ . A supercontinuum light source (NKT photonics, SuperK Extreme) is used to generate spatially coherent ultra-broadband light that is coupled into a single mode fiber (SMF) to the interferometer. Line illumination of the sample with a power of  $\sim 10 \text{ mW}$  is achieved using a plano-convex cylindrical lens (CL). Due to the Gaussian-shaped profile of the illumination in the direction of the line, the illumination is not uniform over the field of view. This effect is corrected by digital post-processing of the acquired images. Light from the sample and reference arms is recombined by a beam splitter (BS) and imaged, using a 200mm-focal

length tube lens (TL), onto a 2048 pixel, 12 bit, line scan CCD camera (e2v, AViiVA EM4). This camera has square pixels of size 14  $\mu\text{m}$  and the line acquisition rate is 70 kHz. The whole reference arm of the interferometer is mounted on a piezoelectric-driven linear stage (PZT1) (Physik Instrument, P625.1CD). The microscope objective in the sample arm is attached to another identical piezoelectric-driven linear stage (PZT2) to adjust the focus in the sample while the reference arm length is scanned. Both stages oscillate in a triangular manner. To ensure that the coherence plane (plane of zero optical path difference) and the focal plane of the objective in the sample arm (MO2) always match, the oscillation amplitudes of the piezoelectric-driven linear stages have to be adjusted depending on the optical refractive indices of the sample and immersion medium (IM). In order to focus at a depth  $z$  below the surface of the sample, starting from focusing at the surface, the microscope objective (MO2) has to be displaced axially towards the sample of a distance [28]

$$d_{obj} = z(n_{im} / n), \quad (1)$$

where  $n_{im}$  and  $n$  are the optical refractive indices of the immersion medium and sample, respectively. To ensure that the coherence plane and the focus match, the length of the reference arm must then be elongated by

$$d_{ref} = z(n^2 - n_{im}^2 + n_{im}) / n. \quad (2)$$

The ratio of the oscillation amplitudes of the stages is therefore

$$d_{ref} / d_{obj} = 1 + (n^2 - n_{im}^2) / n_{im}. \quad (3)$$

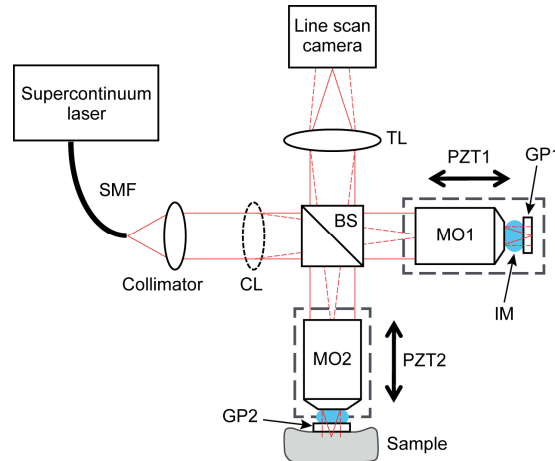


Fig. 1. Schematic of the LC-OCT system. TL: tube lens; PZT: piezoelectric actuator; MO: microscope objective; IM: immersion medium; SMF: single mode fiber; BS: beam-splitter; CL: cylindrical lens. GP: glass plate. The plain red lines represent the beam in the plane of the figure (the cylindrical lens has no effect in this plane). The dotted red lines represent the beam in the direction orthogonal to the plane of the figure.

If the immersion medium and the sample have different optical dispersion properties, a mismatch of the optical dispersion occurs in the interferometer arms as the imaging depth is increased. This leads to a progressive degradation with depth of the axial resolution and contrast of the image [28]. To minimize this phenomenon, an immersion medium with an optical dispersion as close as possible to that of the sample is chosen. Silicone oil ( $n_{im} \approx 1.40$ ) rather than water is used as the immersion medium for better matching of the biological tissue refractive index properties. According to Eq [3], the displacements of both linear stages are

then identical ( $d_{obj} = d_{ref}$ ). The experimental setup could then be simplified using a single piezoelectric-driven linear stage to displace the whole interferometer [28,29]. However, increasing the mass to be moved would limit the imaging speed due to higher inertia. The use of two piezoelectric stages instead of only one reduces the mass to be moved. In addition, in the case of a sample with a refractive index different from that of the immersion medium, our experimental setup would still allow the coherence and focus planes to match throughout the depth scan to ensure optimal image quality.

A phase-shifting algorithm is applied to extract the fringe envelope from the acquired interferometric data. We have chosen an algorithm that requires the combination of five lines,  $(E_1, E_2, E_3, E_4, E_5)$ , according to  $(E_4 - E_2)^2 - (E_1 - E_3)(E_3 - E_5)$ , with a phase shift of  $\pi/2$  between two consecutive lines [30]. This algorithm that can be represented as a second-order nonlinear filter is known to be near optimal in terms of computational efficiency and accuracy in the presence of miscalibration [30]. The translation speed of the piezoelectric-driven linear stages is adjusted so that an optical phase-shift of  $\sim \pi/2$  is generated in the interferometer between the acquisitions of two consecutive lines. Assuming that  $n \approx n_{im}$ , the displacement of both stages between the acquisitions of two consecutive lines is therefore  $\delta z = \bar{\lambda} / (8n)$ , where  $\bar{\lambda}$  denotes the central optical wavelength of the detected light. The number  $N$  of lines acquired by the camera over the whole travel range  $\Delta z$  of the piezo stages is  $N = \Delta z / \delta z$ . With  $\bar{\lambda} = 800$  nm,  $n = 1.4$  and  $\Delta z = 500$   $\mu\text{m}$ , the value of  $N$  is 7000. A stack of 7000 lines is thus acquired during a depth scan of the sample over a 500- $\mu\text{m}$  stroke. An intensity-based B-scan image of the sample is obtained by processing the acquired stack using the fringe envelope detection algorithm mentioned above. Acquisition and processing of stacks is repeated during the round-trips of the piezo stages. The camera operating at its maximal frequency of 70 kHz, the piezo stages oscillate in a triangular manner at a frequency of 70 kHz / 7000 = 10 Hz. The calculation of the B-scan images is performed with a field-programmable gate array (FPGA). The images are displayed in real-time at 10 frames/s in logarithmic scale with auto-adjusted contrast after being appropriately rescaled. The size of each B-scan is 2048  $\times$  875 pixels (lateral  $\times$  axial), corresponding to a field of view of 1.2 mm  $\times$  0.5 mm (lateral  $\times$  axial). Image averaging and smoothing can possibly be performed to reduce noise.

Our imaging system is limited in speed by the frame rate of the line scan camera and not by the oscillation of the piezo stages. For the user's ear, the oscillation of the piezo stages at 10 Hz does not generate acoustic noise. Possible artifacts in the images due to mechanical vibrations transmitted to the entire device have not been observed.

### 3. System performance characterization

#### 3.1 Spatial resolution

The lateral resolution of the images depends on the numerical aperture of the microscope objectives. Here, we use microscope objectives of  $NA = 0.5$ . With these objectives, the size of the imaging lateral field is 1.2 mm. In order to measure the lateral resolution, a sharp edge was imaged. We define the lateral resolution of the images as the 20%-80% width of the intensity profile of the measured edge (see Fig. 2(a)) [31]. A value of  $1.3 \mu\text{m} \pm 0.1 \mu\text{m}$  was measured. To our knowledge, this is the best lateral resolution ever achieved with an OCT device capable of real-time B-scan imaging at around 800 nm central wavelength.

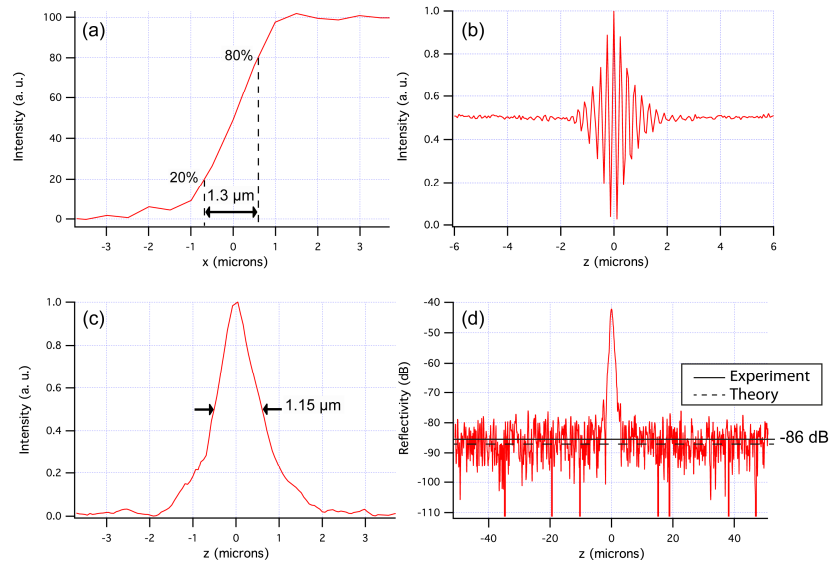


Fig. 2. Measurements of spatial resolution and detection sensitivity. (a) Edge response. (b) Typical interference signal acquired by a pixel of the line-scan camera using a plane interface as a sample. (c) Axial response to a plane interface, obtained from digital demodulation of the interference fringes shown in (b). (d) Axial response to a weak reflectivity ( $8 \times 10^{-5}$ ) plane interface, calibrated in reflectivity and plotted in decibels (dB). The measured noise-floor (plain black line), defined as the detection sensitivity, is compared with the theoretical sensitivity of a hypothetical shot-noise limited detection (dashed black line).

The axial response of the LC-OCT system was measured by imaging the interface between the glass plate (GP2) and air in the sample arm, without sample. The FWHM of the imaged interface was  $1.15 \mu\text{m} \pm 0.01 \mu\text{m}$ , which is considered to be the axial imaging resolution (Fig. 2(c)). This is similar to the best axial resolution reported so far in OCT at a central optical wavelength around 800 nm [8]. The axial and lateral resolutions are close, which is desirable for B-scan imaging.

### 3.2 Detection sensitivity

The detection sensitivity, defined as the smallest detectable reflectivity, was considered to be the mean value of the background noise in the images (see Fig. 2(d)). It can be expressed as an equivalent reflectivity coefficient by comparison with the signal measured from an interface with a known reflectivity. Using the plane interface between the glass window (GP2) and paraffin oil as a calibration sample with a reflectivity of  $\sim 8 \times 10^{-5}$ , the detection sensitivity was evaluated at  $-86 \text{ dB}$ , which is close to the theoretical value of  $-88 \text{ dB}$  assuming a shot-noise limited detection [32].

The line illumination and line detection implemented in LC-OCT, associated with the use of a high-NA microscope objective to image the sample, provide an efficient confocal gate that prevents most unwanted scattered light from being detected. The benefit of confocal gating in LC-OCT was studied by comparing line illumination and full-field illumination. Full-field illumination was achieved by replacing the fibered supercontinuum laser, the collimator and the cylindrical lens by a halogen Köhler illuminator. In this full-field illumination mode, there is no confocal gate. The power spectral distribution of light detected by the camera was similar with both light sources since it was essentially determined by the spectral response of the detector. The brightness of the supercontinuum laser being considerably larger than that of the halogen lamp, light from the supercontinuum laser was attenuated and the camera frame rate was reduced so that the camera could work close to saturation with the same acquisition time and frame rate in both illumination modes. The

camera frame rate being reduced from 70 kHz to 1 kHz, the time to acquire a B-scan image was then 7s, too long for *in vivo* imaging. A laser-viewing card (Thorlabs VRC5) was considered as a static test sample to compare imaging with both illumination modes. Results are shown in Fig. 3. The images are very similar in term of spatial resolution. A significant difference, however, can be observed in the image contrast and in the depth of penetration. The larger amount of incoherent scattered light with full-field illumination compared to line illumination reduces the maximum usable optical power before the camera saturates. The detection sensitivity and hence the image contrast and penetration depth are therefore improved with line illumination. This experiment confirms the advantage of line illumination over full-field illumination, as already reported in a line-scanning optical coherence microscopy (OCM) device designed for *en face* imaging [33]. The confocal gate with line illumination, although less efficient than the confocal gate achieved with point illumination [34], is beneficial compared to the absence of confocal gate, which is a known disadvantage of the full-field OCT/OCM technique [33–37]. The beneficial effect of confocal filtering of unwanted scattered light, illustrated here by imaging an infrared viewing card, is expected to be even more important for the imaging of biological tissues that are more scattering.

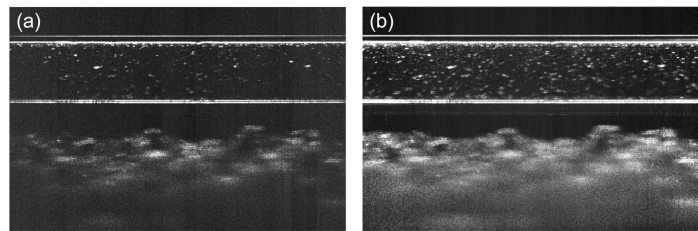


Fig. 3. LC-OCT B-scan images of an infrared viewing card with full-field illumination (a) and line-field illumination (b). Scale bar: 100  $\mu\text{m}$ .

It has been shown theoretically and experimentally that a degradation of the lateral resolution of the image in full-field and line-field OCT occurs when spatially coherent light is used due to coherent optical cross-talk [38–41]. However, a spatially coherent light source is required in LC-OCT in order to illuminate the sample with the finest possible line of light for efficient confocal gating and with an optical intensity high enough to image at high speed. Besides, according to Fig. 3, a difference in resolution between the image acquired with low spatial coherence illumination (Fig. 3(a)) and the one obtained with high spatial coherence (Fig. 3(b)) is not noticeable at this scale. The blurry background signal deep in the laser-viewing card in Fig. 3(b) suggests that multiple scattering is significant. The comparison with the image obtained with low spatial coherence light (Fig. 3(a)) cannot be done due of insufficient imaging penetration. In practice, for the imaging of biological tissues including the skin, multiple scattering and cross-talk effects do not seem to generate major artifacts in the images, as can be seen in Fig. 4 in the next section.

### 3.4 Application to *in vivo* imaging

In our LC-OCT prototype, each line of a B-scan image is calculated from 5 successive interferometric line images acquired by the line scan camera. The time required to calculate each line (of 2048 pixels) of a B-scan image is therefore equal to  $5 / f_{\text{camera}} = 71 \mu\text{s}$ , where  $f_{\text{camera}} = 70 \text{ kHz}$  is the frame rate of the line scan camera. This acquisition time of a few tens of microseconds is similar to the acquisition time of each column (A-scan) of a B-scan image in conventional FD-OCT [42]. It is short enough to avoid blurring of the phase-sensitive interferometric signal that may occur due to sample motion. In LC-OCT, however, motion may result in image distortion due to the relatively low image acquisition rate (10 Hz). These artifacts are avoided by the mechanical stabilization achieved by pressing the sample against a glass plate maintained at a fixed position under the microscope objective (GP2 in Fig. 1). B-

scan imaging at rates of several kHz has been demonstrated using FD-OCT devices with point illumination [43,44] and line-field illumination [45,46]. These ultrahigh-speed FD-OCT devices, however, produce images with lower spatial resolution compared to LC-OCT. As explained previously, the aim of the parallelization of the A-scan acquisition in LC-OCT is to allow a reduction of the speed of the axial scan without slowing down the B-scan acquisition rate. Axial scanning at a frequency of only a few Hz makes possible continuous dynamic focusing of a microscope objective in order to image with high lateral resolution.

Human skin was imaged *in vivo* to illustrate the performance of LC-OCT. A drop of paraffin oil was added on the skin before it was pressed against the glass window to provide index matching and thus minimize the reflection of light at the interfaces. Figure 4 shows an example image of healthy skin obtained from a 25-year-old man on the palm and the back of the hand. Both images are the result of an average of 4 B-scans followed by a Gaussian smoothing with a width (standard deviation) of 1 pixel. The epidermis and the dermis can be clearly distinguished. They are separated by the dermal-epidermal junction (DEJ). Several layers can be identified in the epidermis: the stratum corneum, the stratum granulosum, the stratum spinosum, and the stratum basale. The nuclei of keratinocyte cells (K) in the epidermis are resolved and appear as black spots in the image. Collagen fibers (CF) and blood vessels (BV) can be distinguished in the dermis. Other structures such as a hair (H) and a sweat duct (SD) can be observed.

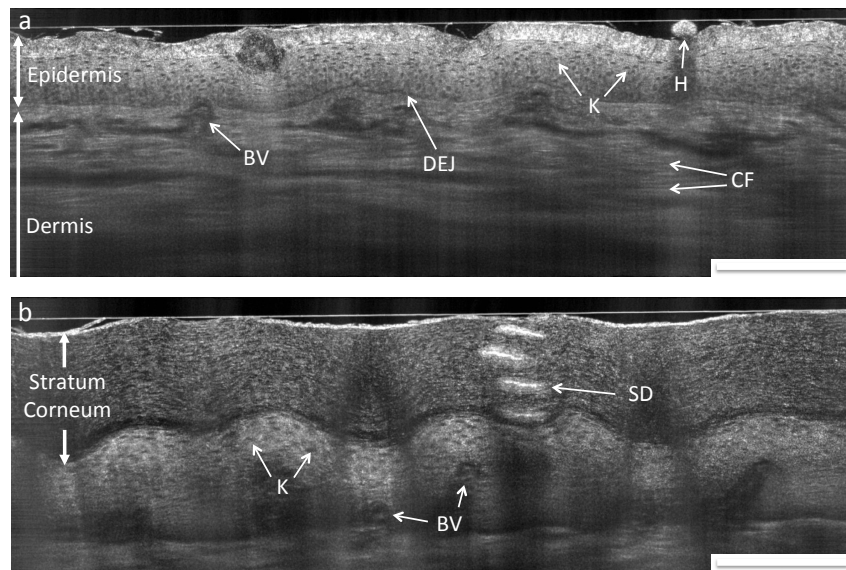


Fig. 4. LC-OCT B-scan images of human skin, *in vivo*. Back (a) and palm (b) of the hand. K: keratinocytes; DEJ: dermal-epidermal junction; SD: sweat duct; H: hair; CF: collagen fibers; BV: blood vessels. Scale bars: 200  $\mu\text{m}$ .

#### 4. Conclusion

We have introduced line-field confocal optical coherence tomography (LC-OCT), a parallelized time-domain OCT technique designed for ultrahigh-resolution B-scan imaging in real time. By using a supercontinuum laser as the light source and 0.5-NA dynamically-focused microscope objective, a quasi-isotropic spatial resolution of  $\sim 1 \mu\text{m}$  is obtained. The similarity of the axial and lateral resolutions is of particular importance for B-scan imaging. The confocal gate achieved by line illumination and detection along with the use of a relatively high-NA microscope objective to image the sample has a beneficial effect on the signal detection, which directly impacts the image contrast and penetration. *In vivo* cellular-level imaging in skin has been demonstrated using LC-OCT at 10 fps without motion

artifacts. LC-OCT could be of particular interest for biological and medical applications requiring a non-invasive technique that provides cross-sectional images in real-time with a resolution close to that of histology.

The frame rate of 10 Hz reported here for B-scan imaging could be increased without reducing the detection sensitivity by using a faster line scan camera with a similar dynamic range, provided that the power of the laser source could be increased to fill the full well capacity of the camera without damaging the sample and that the piezo stages could oscillate at a higher frequency. With the technologies currently available, we estimate that the frame rate in LC-OCT could be increased by a factor of about 3. Three-dimensional (3D) imaging with LC-OCT may be possible by scanning the illumination line laterally to acquire a stack of B-scans recorded at different lateral positions. 3D imaging with LC-OCT would probably be difficult to achieve in real-time but would have the advantage of very high ( $\sim 1 \mu\text{m}$ ) isotropic spatial resolution.

### Funding

“Initiative D’EXcellence (IDEX) Paris-Saclay” (Innovation et Entrepreneuriat, phase prématuration); “Aide à la MAturation de projets innovants” (AIMA) Région Île de France & Bpifrance; and “ASTRE” (Action de Soutien à la Technologie et la Recherche en Essonne).

### References

1. D. Huang, E. A. Swanson, C. P. Lin, J. S. Schuman, W. G. Stinson, W. Chang, M. R. Hee, T. Flotte, K. Gregory, C. A. Puliafito, and J. G. Fujimoto, “Optical coherence tomography,” *Science* **254**(5035), 1178–1181 (1991).
2. A. F. Fercher, “Optical coherence tomography,” *J. Biomed. Opt.* **1**(2), 157–173 (1996).
3. A. M. Zysk, F. T. Nguyen, A. L. Oldenburg, D. L. Marks, and S. A. Boppart, “Optical coherence tomography: a review of clinical development from bench to bedside,” *J. Biomed. Opt.* **12**(5), 051403 (2007).
4. J. S. Schuman, C. A. Puliafito, J. G. Fujimoto, and J. S. Duker, *Optical Coherence Tomography of Ocular Diseases*, 3rd ed. (Slack Inc., Thorofare, NJ, 2013).
5. H. G. Bezerra, M. A. Costa, G. Guagliumi, A. M. Rollins, and D. I. Simon, “Intracoronary optical coherence tomography: A Comprehensive Review,” *JACC Cardiovasc. Interv.* **2**(11), 1035–1046 (2009).
6. D. C. Adler, Y. Chen, R. Huber, J. Schmitt, J. Connolly, and J. G. Fujimoto, “Three-dimensional endomicroscopy using optical coherence tomography,” *Nat. Photonics* **1**(12), 709–716 (2007).
7. A. Levine, K. Wang, and O. Markowitz, “Optical coherence tomography in the diagnosis of skin cancer,” *Dermatol. Clin.* **35**(4), 465–488 (2017).
8. W. Drexler, U. Morgner, F. X. Kärtner, C. Pitris, S. A. Boppart, X. D. Li, E. P. Ippen, and J. G. Fujimoto, “In vivo ultrahigh-resolution optical coherence tomography,” *Opt. Lett.* **24**(17), 1221–1223 (1999).
9. B. Povazay, K. Bizheva, A. Unterhuber, B. Hermann, H. Sattmann, A. F. Fercher, W. Drexler, A. Apolonski, W. J. Wadsworth, J. C. Knight, P. S. J. Russell, M. Vetterlein, and E. Scherzer, “Submicrometer axial resolution optical coherence tomography,” *Opt. Lett.* **27**(20), 1800–1802 (2002).
10. Y. Wang, Y. Zhao, J. S. Nelson, Z. Chen, and R. S. Windeler, “Ultrahigh-resolution optical coherence tomography by broadband continuum generation from a photonic crystal fiber,” *Opt. Lett.* **28**(3), 182–184 (2003).
11. A. Aguirre, N. Nishizawa, J. Fujimoto, W. Seitz, M. Lederer, and D. Kopf, “Continuum generation in a novel photonic crystal fiber for ultrahigh resolution optical coherence tomography at 800 nm and 1300 nm,” *Opt. Express* **14**(3), 1145–1160 (2006).
12. R. A. Leitgeb, M. Villiger, A. H. Bachmann, L. Steinmann, and T. Lasser, “Extended focus depth for Fourier domain optical coherence microscopy,” *Opt. Lett.* **31**(16), 2450–2452 (2006).
13. K. S. Lee and J. P. Rolland, “Bessel beam spectral-domain high-resolution optical coherence tomography with micro-optic axicon providing extended focusing range,” *Opt. Lett.* **33**(15), 1696–1698 (2008).
14. J. Mo, M. de Groot, and J. F. de Boer, “Focus-extension by depth-encoded synthetic aperture in Optical Coherence Tomography,” *Opt. Express* **21**(8), 10048–10061 (2013).
15. T. S. Ralston, D. L. Marks, P. S. Carney, and S. A. Boppart, “Interferometric synthetic aperture microscopy,” *Nat. Phys.* **3**(2), 129–134 (2007).
16. L. Yu, B. Rao, J. Zhang, J. Su, Q. Wang, S. Guo, and Z. Chen, “Improved lateral resolution in optical coherence tomography by digital focusing using two-dimensional numerical diffraction method,” *Opt. Express* **15**(12), 7634–7641 (2007).
17. D. J. Fechtig, A. Kumar, W. Drexler, and R. A. Leitgeb, “Full range line-field parallel swept source imaging utilizing digital refocusing,” *J. Mod. Opt.* **62**(21), 1801–1807 (2015).
18. S. Liu, J. A. Mulligan, and S. G. Adie, “Volumetric optical coherence microscopy with a high space-bandwidth-time product enabled by hybrid adaptive optics,” *Biomed. Opt. Express* **9**(7), 3137–3152 (2018).

19. J. P. Rolland, P. Meemon, S. Murali, K. P. Thompson, and K.-S. Lee, "Gabor-based fusion technique for optical coherence microscopy," *Opt. Express* **18**(4), 3632–3642 (2010).
20. J. Holmes and S. Hattersley, "Optical coherence tomography and coherence domain optical methods in biomedicine XIII," *Proc. SPIE* **7168**, 71681N (2009).
21. J. M. Schmitt, S. L. Lee, and K. M. Yung, "An optical coherence microscope with enhanced resolving power in thick tissue," *Opt. Commun.* **142**(4-6), 203–207 (1997).
22. F. Lexter, C. K. Hitzenberger, W. Drexler, S. Molebny, H. Sattmann, M. Sticker, and A. F. Fercher, "Dynamic coherent focus OCT with depth-independent transversal resolution," *J. Mod. Opt.* **46**(3), 541–553 (1999).
23. B. Qi, P. A. Himmer, M. L. Gordon, V. X. D. Yang, D. L. Dickensheets, and I. A. Vitkin, "Dynamic focus control in high-speed optical coherence tomography based on a microelectromechanical mirror," *Opt. Commun.* **232**(1-6), 123–128 (2004).
24. A. Divetia, T.-H. Hsieh, J. Zhang, Z. Chen, M. Bachman, and G.-P. Li, "Dynamically focused optical coherence tomography for endoscopic applications," *Appl. Phys. Lett.* **86**(10), 103902 (2005).
25. V. X. D. Yang, N. Munce, J. Pekar, M. L. Gordon, S. Lo, N. E. Marcon, B. C. Wilson, and I. A. Vitkin, "Micromachined array tip for multifocus fiber-based optical coherence tomography," *Opt. Lett.* **29**(15), 1754–1756 (2004).
26. A. G. Podoleanu, J. A. Rogers, D. A. Jackson, and S. Dunne, "Three dimensional OCT images from retina and skin," *Opt. Express* **7**(9), 292–298 (2000).
27. M. J. Cobb, X. Liu, and X. Li, "Continuous focus tracking for real-time optical coherence tomography," *Opt. Lett.* **30**(13), 1680–1682 (2005).
28. A. Dubois, "Focus defect and dispersion mismatch in full-field optical coherence microscopy," *Appl. Opt.* **56**(9), D142–D150 (2017).
29. J. Ogien and A. Dubois, "A compact high-speed full-field optical coherence microscope for high-resolution in vivo skin imaging," *J. Biophotonics* **2018**, e201800208 (2018).
30. K. G. Larkin, "Efficient nonlinear algorithm for envelope detection in white light interferometry," *J. Opt. Soc. Am. A* **13**(4), 832–843 (1996).
31. Y. S. Sabharwal, A. R. Rouse, L. Donaldson, M. F. Hopkins, and A. F. Gmitro, "Slit-scanning confocal microendoscope for high-resolution in vivo imaging," *Appl. Opt.* **38**(34), 7133–7144 (1999).
32. *Optical Coherence Tomography, Technology and Applications*, W. Drexler and G. Fujimoto, eds. (Springer, 2008), Chap. 19, p. 565–592, Full-Field Optical Coherence Tomography, A. Dubois and A. C. Boccara.
33. Y. Chen, S.-W. Huang, A. D. Aguirre, and J. G. Fujimoto, "High-resolution line-scanning optical coherence microscopy," *Opt. Lett.* **32**(14), 1971–1973 (2007).
34. Y. Chen, S. W. Huang, C. Zhou, B. Potsaid, and J. G. Fujimoto, "Improved Detection Sensitivity of Line-Scanning Optical Coherence Microscopy," *IEEE J. Sel. Top. Quantum Electron.* **18**(3), 1094–1099 (2012).
35. L. Vabre, A. Dubois, and A. C. Boccara, "Thermal-light full-field optical coherence tomography," *Opt. Lett.* **27**(7), 530–532 (2002).
36. A. Dubois, *Handbook of Full-Field Optical Coherence Microscopy, Technology and Applications*, A. Dubois eds., (Pan Stanford Publishing Singapore 2016), Chap. 1, p. 1–51.
37. M. J. Yadlowsky, J. M. Schmitt, and R. F. Bonner, "Multiple scattering in optical coherence microscopy," *Appl. Opt.* **34**(25), 5699–5707 (1995).
38. Q. Lu, X. Gan, M. Gu, and Q. Luo, "Monte Carlo modeling of optical coherence tomography imaging through turbid media," *Appl. Opt.* **43**(8), 1628–1637 (2004).
39. B. Karamata, P. Lambelet, M. Laubscher, R. P. Salathé, and T. Lasser, "Spatially incoherent illumination as a mechanism for cross-talk suppression in wide-field optical coherence tomography," *Opt. Lett.* **29**(7), 736–738 (2004).
40. B. Karamata, M. Leutenegger, M. Laubscher, S. Bourquin, T. Lasser, and P. Lambelet, "Multiple scattering in optical coherence tomography. II. Experimental and theoretical investigation of cross talk in wide-field optical coherence tomography," *J. Opt. Soc. Am. A* **22**(7), 1380–1388 (2005).
41. B. Grajciar, M. Pircher, A. Fercher, and R. Leitgeb, "Parallel Fourier domain optical coherence tomography for in vivo measurement of the human eye," *Opt. Express* **13**(4), 1131–1137 (2005).
42. S. H. Yun, G. Tearney, J. de Boer, and B. Bouma, "Motion artifacts in optical coherence tomography with frequency-domain ranging," *Opt. Express* **12**(13), 2977–2998 (2004).
43. T. Wang, T. Pfeiffer, E. Regar, W. Wieser, H. van Beusekom, C. T. Lancee, G. Springeling, I. Krabbendam, A. F. W. van der Steen, R. Huber, and G. van Soest, "Heartbeat OCT: in vivo intravascular megahertz-optical coherence tomography," *Biomed. Opt. Express* **6**(12), 5021–5032 (2015).
44. K. L. Lurie, A. A. Gurjarpadhye, E. J. Seibel, and A. K. Ellerbee, "Rapid scanning catheterscope for expanded forward-view volumetric imaging with optical coherence tomography," *Opt. Lett.* **40**(13), 3165–3168 (2015).
45. D. J. Fechtig, B. Grajciar, T. Schmoll, C. Blatter, R. M. Werkmeister, W. Drexler, and R. A. Leitgeb, "Line-field parallel swept source MHz OCT for structural and functional retinal imaging," *Biomed. Opt. Express* **6**(3), 716–735 (2015).
46. L. Ginner, A. Kumar, D. Fechtig, L. M. Wurster, M. Salas, M. Pircher, and R. A. Leitgeb, "Noniterative digital aberration correction for cellular resolution retinal optical coherence tomography in vivo," *Optica* **4**(8), 924–931 (2017).